

# Geophysical Research Letters

## RESEARCH LETTER

10.1029/2020GL087378

### Key Points:

- We present a new method combining laser ultrasonics with DEM modeling to separate effects of microfractures from mineral foliation
- Microfracture porosity is generally small at the Alpine Fault but increases toward the principal slip zone
- Up to 40% of fractures are aligned with the foliation in the schist and mylonites while fractures are randomly oriented in the cataclasite

### Supporting Information:

- Supporting Information S1

### Correspondence to:

J. Simpson,

jsim921@aucklanduni.ac.nz

### Citation:

Simpson, J., Adam, L., van Wijk, K., & Charoensawan, J. (2020).

Constraining microfractures in foliated alpine fault rocks with laser ultrasonics. *Geophysical Research Letters*, 47, e2020GL087378. <https://doi.org/10.1029/2020GL087378>

Received 4 FEB 2020

Accepted 31 MAR 2020

Accepted article online 9 APR 2020

## Constraining Microfractures in Foliated Alpine Fault Rocks With Laser Ultrasonics

**Jonathan Simpson<sup>1</sup> , Ludmila Adam<sup>2</sup> , Kasper van Wijk<sup>1</sup> , and Jirapat Charoensawan<sup>2</sup>**

<sup>1</sup>Dodd-Walls Centre for Photonic and Quantum Technologies and The Physical Acoustics Laboratory, Department of Physics, University of Auckland, Auckland, New Zealand, <sup>2</sup>Physics of Rocks Laboratory, School of Environment, University of Auckland, Auckland, New Zealand

**Abstract** Quantifying the amount and alignment of microfractures is important to understand the geomechanics, fluid flow, and seismic imaging of fault zones. At the Alpine Fault, New Zealand, the preferred alignment of minerals, foliation, and fractures results in elastic wave anisotropy. We have designed a unique laser-ultrasonic laboratory setup to study Alpine Fault rock samples at upper crustal conditions. Combined with differential effective medium modeling, we distinguish microfracture porosity and orientation from mineral alignment, as a function of distance to the principal slip zone (PSZ). Nearest to the PSZ, the cataclasite has the lowest  $P$  wave anisotropy with the most (randomly oriented) fractures. Next, the ultramylonite exhibits the greatest  $P$  wave anisotropy (~45%) with 40% of its fractures aligned with foliation. Further from the PSZ,  $P$  wave anisotropy is 14–19% on average, due to 20–30% of the fractures being oriented in the same direction as mineral alignment.

**Plain Language Summary** The movement on faults causes fractures and alignment of minerals in the adjacent rocks. This causes seismic waves to travel fastest parallel to these features, a phenomenon known as anisotropy. Quantifying the amount and orientation of the fractures that contribute to this anisotropy is important for understanding fault zones and the processes which could influence the nature of earthquakes. However, this requires a method that can separate the effects of the fractures from those of the minerals. We have designed a system that uses laser ultrasonics to measure the speed of waves through rocks under pressure at spatially dense locations. We combine these measurements with numerical modeling, allowing us to accurately quantify the amount and orientation of fractures in rocks from the Alpine Fault, New Zealand. We find that the total amount of fractures increases toward the fault. Additionally, the amount of fractures aligned with the fault plane (up to 40%) increases toward the fault until the fractures become almost completely randomly oriented for the cataclasite in the core of the fault.

## 1. Introduction

Microfractures and macrofractures control rock strength (Scholz, 1968; Walsh & Brace, 1964) and fluid flow (Mitchell & Faulkner, 2012; Walsh, 1981) and influence geophysical imaging of fault zones (Ben-Zion, 1998; Li et al., 1990; Mooney & Ginzburg, 1986). Characterizing their orientation, porosity, and effect on elastic wave anisotropy is vital to understand fault evolution and to develop subsurface fault models. The orientation of microfractures can be related to the distribution of the local stress field and the fault damage zone (Barton et al., 1995; Williams et al., 2018). The orientation and porosity of open microfractures affect permeability and movement of fluids in the subsurface (Barton et al., 1995). This is particularly important around fault zones where the presence of fluids and mineral precipitation are key factors in estimating fault strength (Hubbert & Rubey, 1959; Warr & Cox, 2001).

As fault displacement increases, so does the thickness of the damaged fault zone (Faulkner et al., 2003; Li et al., 1990; Savage & Brodsky, 2011; Shipton et al., 2006). Most of these studies visually identify macrofractures on core or outcrop. The combination of macrofractures and microfractures is extrapolated at depth by identifying seismic low-velocity zones using fault-zone guided waves (FZGWs; Ben-Zion, 1998; Cochran et al., 2009; Li et al., 1990, 2004). However, estimating fracture orientation and porosity near the fault is challenging from FZGWs. In addition, rocks formed within fault shear zones develop strong intrinsic elastic anisotropy from the alignment of platy minerals (such as mica) and foliation (Christensen, 1965; Jones & Nur, 1982; Shea & Kronenberg, 1993). The combined effects of seismic anisotropy and mechanical

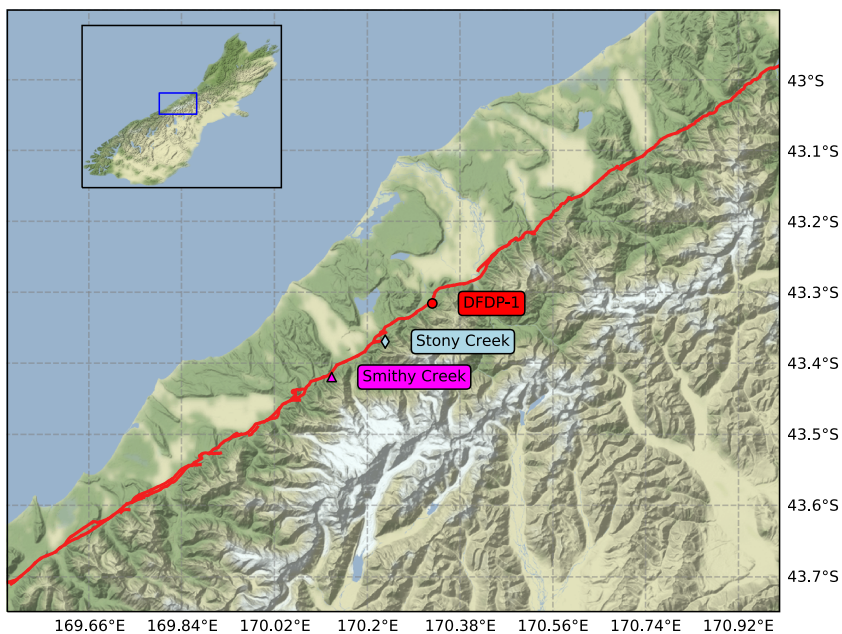


**Figure 1.** The Alpine Fault traverses the South Island of New Zealand. The NE-SW trending fault trace is shown in red (data from the GNS Science Active Faults Database; Langridge et al., 2016), and the symbols indicate the locations where rock samples were collected.

damage result in nonunique solutions when attempting to constrain the fault structure and physical properties from seismic waves (Dempsey et al., 2011; Gulley et al., 2017; Kelly et al., 2017).

We have designed experiments to unravel microfractures from mineral alignment in fault rocks, with a combination of dense ultrasonic velocity measurements and effective medium modeling that is based on estimates of mineral phase distribution and orientation. Estimates of wave speeds are acquired as a function of angle and effective pressures representing shallow crustal depths (<1,000 m) with a newly developed laser ultrasonics system (Simpson et al., 2019). Samples are from five hanging-wall lithologies with increasing distance from the principal slip zone (PSZ) of the Alpine Fault. In these samples we are able to establish the elastic wave anisotropy symmetry and quantitatively distinguish the effects of microfracture porosity, shape, and orientation from the contribution of anisotropic minerals to the total wave speed anisotropy.

The Alpine Fault is a major plate boundary transform fault and geomorphological structure in the South Island of New Zealand. The fault extends for 600 km on land, accommodating slip between the Pacific and Australian plates (Figure 1; Norris & Cooper, 2001; Wellman, 1955). Motion on the fault is predominantly dextral strike slip with a component of reverse faulting toward the northwest, resulting in the uplift of the Southern Alps to the east of the fault (Norris et al., 1990). The fault slips at an average rate of  $27 \pm 5$  mm/year, generating earthquakes of up to magnitude  $M_w 8.0$  at an average recurrence interval of  $\sim 300$  years, with the last such event occurring in 1717 CE (Cochran et al., 2017; Wells et al., 1999). In recent years, the Alpine Fault has been the focus of international multidisciplinary studies aiming to understand the characteristics and processes of a globally significant plate boundary fault late in its interseismic cycle (e.g., Allen et al., 2017; Boulton et al., 2014; Carpenter et al., 2014; Sutherland et al., 2017; Townend et al., 2009; Toy et al., 2013, 2015; Williams et al., 2016, 2018). Three boreholes have been drilled into the Alpine Fault between 2011 and 2014 as part of the Deep Fault Drilling Project (DFDP), with the primary aim of understanding the in situ geophysical conditions and rock properties of the Alpine Fault (Sutherland et al., 2017; Townend et al., 2009). Here, we study one sample from a DFDP borehole along with four samples taken from outcrops.

## 2. Samples and Methods

We investigate five rock samples representative of the different hanging-wall lithologies of the Alpine Fault (Figure 2). In order of decreasing proximity to the PSZ, these samples are a schist, a protomylonite,

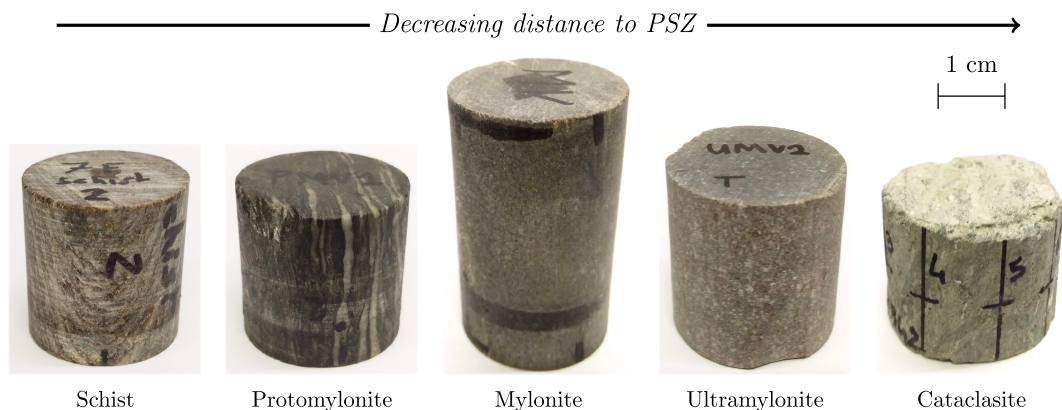


**Figure 2.** Photographs of the five rock samples investigated in this study. All samples are taken from surface outcrops except the cataclasite, which is from the DFDP-1A borehole.

a mylonite, an ultramylonite, and a cataclasite. Perpendicular to the PSZ of the Alpine Fault, cataclasites and ultramylonites extend up to 150 m (Sutherland et al., 2015), while the other three lithologies extend for several kilometers from the PSZ. The schist sample comes from a surface outcrop at Smithy Creek and is part of the Alpine Schist tectonostratigraphic unit. The protomylonite, mylonite, and ultramylonite are from a surface outcrop at Stony Creek (Figure 1).

Alpine schist commonly has a planar foliation defined by alternating layers of mica and quartz/feldspar. The protomylonite, mylonite, and ultramylonite units are derived from this quartzo-feldspathic schist, and all share a similar mineralogy and basal plane orientations with varying accessory minerals (complete mineral compositions for these rocks are available in the supporting information). For these rocks, foliation is overprinted by a mylonitic fabric, most obviously manifesting as submillimeter to centimeter-spaced shear bands, which form at depth by ductile creep mechanisms (Gillam et al., 2014; Toy et al., 2012, 2015). Based on observations in the field (Gillam et al., 2014; Norris & Cooper, 1997; Toy et al., 2008, 2017), borehole sonic image logs (Massiot et al., 2018), and core X-ray tomography (Williams et al., 2018), foliation in the upper 1 km of the fault is parallel to the shear zone boundary, dipping at 60° (Toy et al., 2013). Ultramylonites show fine-grained minerals and less obvious bands. Nonetheless, aligned mica bands and lenses are visible in microphotographs (see supporting information). Our samples are similar to those described by Toy et al. (2008, 2012, 2015), differing in the precise modal mineralogy present. Additionally, the porosities of these four samples at atmospheric conditions are all below 5%. Our cataclasite sample is from the drill core obtained from the DFDP-1A borehole at a depth of 84.29 m below the surface in the unit 4 upper foliated cataclasite and 6.7 m above the PSZ (Toy et al., 2015). Its semiquantitative mineralogy determined from X-ray diffraction analysis is 28% quartz, 16% feldspar, 31% micas, 14% chloride, and 10% calcite (Adam et al., 2017). Some foliation is present among comminuted grains and fragments (<1 cm in size), and the sample has a porosity of ~20% at atmospheric conditions.

Samples are prepared for ultrasonic experiments by coring or sculpting 25-mm-diameter cylinders. Visible foliation in the rocks is approximately aligned with the cylinder axis. We dry the rocks in an oven before applying a thin brass and epoxy jacket to prevent the confining gas from entering the pore space. We excite and detect ultrasonic waves with lasers (Blum et al., 2013; Scruby & Drain, 1990; Simpson et al., 2019). A pulse of an Nd:YAG laser generates ultrasonic waves at the surface of the sample. These waves are recorded with a laser Doppler vibrometer, discretized at 10 MS/s, and converted to absolute particle displacement. The source and receiver lasers are aligned on exact opposite sides of the cylindrical rock sample, which is mounted inside a pressure vessel with optical windows. We record over 90 independent waveforms over a range of orientations relative to the anisotropic symmetry axis, rotating each sample through ~160°. These rotational scans are repeated for nine effective pressures between 1 and 16 MPa. *P* wave velocities are estimated from picking the first arrival in each waveform. As an example, recorded wavefields with the *P* wave arrival picks for the ultramylonite are presented in the supporting information.

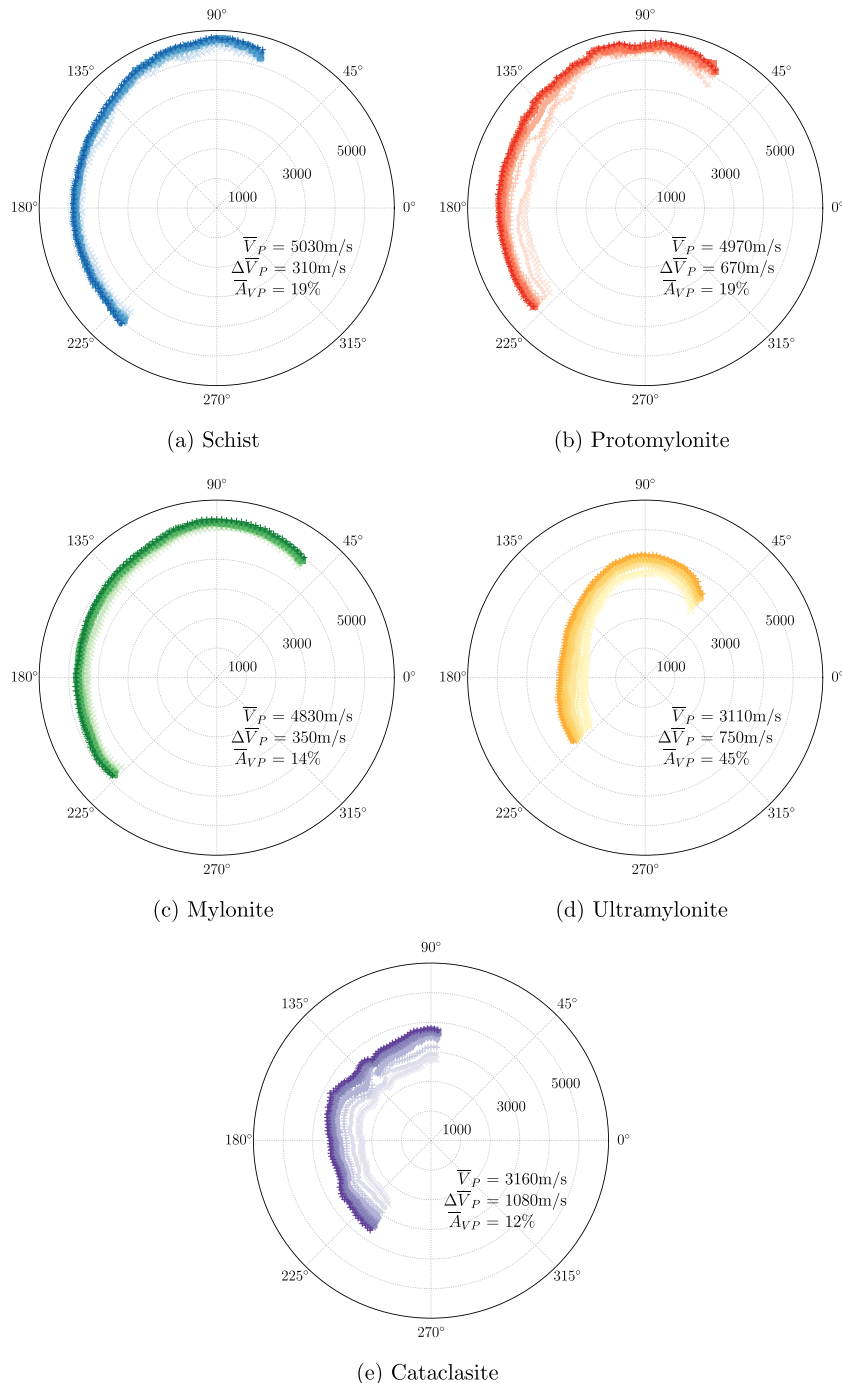


**Figure 3.**  $P$  wave velocity as a function of angle and pressure for all samples. Other than the cataclasite, all samples show a transversely isotropic symmetry. The  $\bar{A}_{VP}$  for the cataclasite (e) is therefore a measure of rock heterogeneity. Darker shades indicate higher pressures, and the radial axis has units of m/s. Total average velocity ( $\bar{V}_P$ ), change in average  $P$  wave velocity between 1 and 16 MPa ( $\Delta\bar{V}_P$ ), and average  $P$  wave anisotropy ( $\bar{A}_{VP}$ ) are stated for each sample.  $P$  wave anisotropy is calculated as  $A_{VP} = (V_f - V_s) / [[V_f + V_s] / 2]$  where  $V_f$  and  $V_s$  are the fast and slow  $P$  wave velocities.

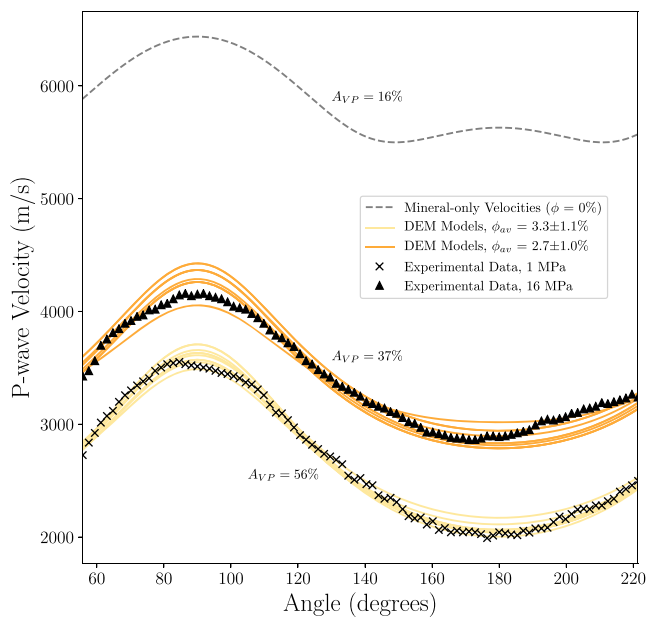


**Figure 4.** Comparison of experimental data with DEM models for the ultramylonite sample. The background mineral-only velocities from EBSD/MTEX modeling are shown for comparison, along with  $P$  wave anisotropies ( $A_{VP}$ ). The 10 models that best fit the experimental data at both 1 and 16 MPa have  $40 \pm 2\%$  of their total fractures aligned with the foliation of the minerals.

### 3. Results

#### 3.1. Laser Ultrasonics Experiments

Wave speeds as a function of angular orientation and pressure are plotted for all samples in Figure 3. The total average wave speed  $\bar{V}_P$  is less in the two samples closest to the fault. All samples except the cataclasite display elliptical angular variation in  $P$  wave speed. For the ultramylonite, the average  $P$  wave anisotropy ( $\bar{A}_{VP} = 45\%$ ) is over twice that of the other samples ( $\bar{A}_{VP} = 12\text{--}20\%$ ). All four of these samples show a decrease in anisotropy with increasing pressure, indicating that the wave speeds in the slow direction are more sensitive to pressure than those in the fast direction. Angular variation of wave speed in the cataclasite shows no clearly defined fast and slow directions. As pressure increases, the wave speed in this sample increases by approximately the same amount in all directions. Finally, the difference between the average wave speeds at 1 and 16 MPa ( $\Delta\bar{V}_P$ ) increases toward the PSZ, indicating that the wave speeds become more sensitive to pressure closer to the fault. The exception to this trend is the large  $\Delta\bar{V}_P$  of the protomylonite, but this is mostly driven by anomalously low wave speeds for this sample around the slow direction ( $180^\circ$ ) at pressures of 1–4 MPa (likely caused by a compliant macroscale fracture).

#### 3.2. DEM Modeling

We use electron backscatter diffraction (EBSD) data of thin sections to estimate the mineral composition and crystal preferred orientations of all samples except the cataclasite. Using these data, we estimate the elastic stiffness matrices of the mineral background medium using the MTEX code (Mainprice et al., 2015). The differential effective medium (DEM) theory proposed by Bruner (1976) is then used to model the bulk elastic properties of the mineral background medium with inclusions (Bruner, 1976; Kim et al., 2019). We vary the amount, orientation, and aspect ratio of these inclusions (microfractures) until the model velocities fit the laser-ultrasonic velocity estimates. Details of the EBSD, MTEX, and modeling methodology, along with complete results, are presented in the supporting information.

Figure 4 shows the 10 best-fitting DEM models for the ultramylonite at both 1 and 16 MPa. Comparison with the mineral-only velocities demonstrates the large reduction in  $P$  wave velocity and increase in anisotropy caused by the microfractures. For the DEM models in Figure 4, the average percentage of fractures aligned with the foliation is  $40 \pm 2\%$ . The total average porosity of the models decreases from  $\phi_{av} = 3.3 \pm 1.1\%$  at 1 MPa to  $\phi_{av} = 2.7 \pm 1.0\%$  at 16 MPa, and the average aspect ratio of the fractures decreases from 88:88:1 to 72:72:1. The average aspect ratios and total porosity of the ultramylonite are greater than those of the other

samples. On average, the schist, protomylonite, and mylonite require 16–30% of the fractures to be aligned with the foliation to satisfactorily model the measured velocities.

#### 4. Discussion

For all rocks, the average measured  $P$  wave velocities over all pressures and orientations (3,110–5,030 m/s) are significantly lower than the average modeled mineral-only velocities (5,830–5,930 m/s). This suggests that all our samples contain microfractures, reducing their bulk stiffness. DEM modeling indicates that fracture porosity is less than 1.3% in the schist, protomylonite, and mylonite. More than twice as much porosity (2.7%) is required to fit the ultramylonite wave speeds. These numbers are corroborated by direct estimates of total porosity of the samples. The average  $P$  wave speeds of the schist (5,030 m/s), protomylonite (4,970 m/s), and mylonite (4,830 m/s) are similar, while those of the ultramylonite (3,110 m/s) and cataclasite (3,160 m/s) are significantly lower. These measurements of  $P$  wave velocity agree with values reported in previous studies of both Alpine Fault schists and mylonites (4,000–6,000 m/s; Christensen & Okaya, 2007), as well as ultramylonites and cataclasites (3,000–4,000 m/s; Townend et al., 2013) under similar conditions. Similar  $P$  wave speeds among the schist, protomylonite, and mylonite indicate that they have similar fracture porosities, while the lower velocities in the ultramylonite and cataclasite suggest that these rocks have higher fracture porosities. Indeed, greater pressure dependence of the laser-ultrasonic wave speeds for the ultramylonite and cataclasite is consistent with higher fracture porosities, compared to the other samples. The ultramylonite and cataclasite lie within the damage zone of the Alpine Fault, which extends ~160 m from the PSZ and has higher fracture densities and lower seismic velocities (Sutherland et al., 2015; Williams et al., 2018). Eccles et al. (2015) show that this low-velocity damage zone explains observed fault-zone guided waves.

The elliptical angular dependence of wave speed confirms that the schist, mylonite, protomylonite, and ultramylonite have a transversely isotropic elastic symmetry. This can be due to foliation and aligned micas, aligned microfractures, or a combination of these. Average  $P$  wave anisotropy for the modeled mineral-only velocities ranges from 13.6% to 16.5% for these samples, lower than the measured average anisotropy values. Additionally, laser-ultrasonic data for all rocks except the cataclasite exhibit a slow wave speed direction more sensitive to pressure than the fast direction, which is aligned with the plane of visible foliation (Figure 3). This means that there is at least a subset of the fracture porosity that is aligned with foliation for the mylonitic and schist samples. By combining laser-ultrasonic measurements under pressure with DEM modeling, we are able to separate the effect of mineral foliation from fractures and quantify fracture shape, porosity, and alignment. We find that 16–40% of planar microfractures must be aligned with foliation to satisfactorily fit the data. Conversely, the lack of an elliptical angular symmetry in wave speeds for the cataclasite indicates that mineral foliation and microfracture alignment have been disrupted by mechanical damage and hydrothermal alteration close to the PSZ. Computed tomography images confirm only remnant foliation and a pore network composed mostly of randomly oriented microfractures and comminuted grain fragments (figure 5.5 of Simpson, 2019).

Open and mineralized macrofractures (>0.5 mm) have been characterized from X-ray tomography (Williams et al., 2017) and sonic image logs (Massiot et al., 2018). For the schists and mylonite sequence intersected by the DFDP-2B borehole, Massiot et al. (2018) point at the existence of a dominant macrofracture set parallel to foliation. This is in agreement with our observations for all lithologies other than the cataclasite (Figure 5). Williams et al. (2018) report that macrofractures are mostly randomly distributed in an inner damage zone less than 160 m from the PSZ, in agreement with our cataclasite observations. While our ultramylonite also lies within this damage zone, we suggest that under high shear stress with proximity to the PSZ, the ultramylonite's enhanced fine-scale foliation could lead to the preferential development of aligned microfractures. It is possible that macrofractures, as those observed by Williams et al. (2018), have a different mechanism of formation. Allen et al. (2017) measure elastic wave anisotropy only at two directions on core samples from the Alpine Fault and discuss that their wave anisotropy estimates are not well constrained due to the limited data. Our method shows how, by obtaining spatially dense estimates of wave speed under effective pressure, anisotropy due to mineral alignment and open microfractures can be separated and quantified.

Our interpretation of microfracture porosity and orientation within the sequence of lithologies extending from the PSZ of the Alpine Fault is summarized in Figure 5. First, microfracture porosity increases with proximity to the PSZ of the Alpine Fault. Second, microfractures are more aligned with foliation and elongated in the ultramylonite, possibly due to enhanced fine-scale foliation closer to the PSZ. Third, although

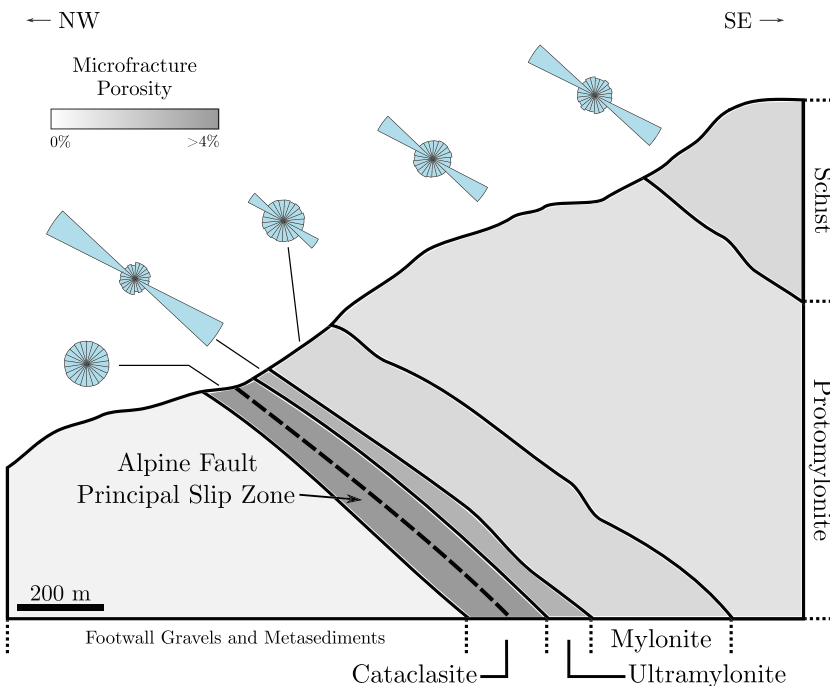


**Figure 5.** Model cross section of the shallow crustal portion of the Alpine Fault representing the degree of microfracture porosity and alignment for effective pressures up to 16 MPa. Rose diagrams represent the orientation of a long axis for microfractures with their short axis in the plane of the cross section. The thicknesses of the different lithological units are approximately to scale (Norris & Cooper, 2007).

aligned fractures are present in mylonitic and schist rocks, randomly oriented fractures are present throughout the Alpine Fault lithologies and contribute to at least 60% of the fracture porosity of the shallow Alpine Fault. Finally, transversely isotropic symmetry of wave speeds is due to foliation, aligned micas, and aligned microfractures. However, within tens of meters from the PSZ, this symmetry is disrupted in the cataclasite due to the geomechanical and geochemical damage close to the PSZ.

## 5. Conclusions

We have quantified the porosity and alignment of microfractures in five rock samples from the shallow Alpine Fault in New Zealand. By combining a new laser-ultrasonic technique with differential effective medium modeling, we could distinguish these microfracture properties from mineral alignment.

We found that the microfracture porosity is generally small (<3%) but increases toward the PSZ. Our analysis identified the percentage of microfractures aligned with the mineral foliation to be 16–30% in schist and mylonites further away from the PSZ. The ultramylonite has the greatest percentage of its fractures aligned with the foliation (~40%) due to stronger shear deformation and greater damage. Within tens of meters of the PSZ, the alignment of minerals and microfractures in the cataclasite is disrupted by fault dynamics. These quantitative estimates of porosity and alignment of microfractures—overprinted on foliation—are important to understand the geomechanics, fluid flow, and seismic imaging of fault zones such as the Alpine Fault.

## Acknowledgments

We thank Shreya Kanakiya for her help with the microphotographs and X-ray diffraction analysis on the cataclasites and Mike Ofman, Virginia Toy, and the University of Otago for their help with the EBSD analysis. We thank the Royal Society of New Zealand, Marsden Contract 14-UOA-028, for partially funding this research. We also thank Jack Williams for his constructive feedback, which helped improve this manuscript. All data and code are available via the DOI <https://doi.org/10.17608/k6.auckland.c.4841352> (Simpson et al., 2020).

## References

- Adam, L., Guerin-Marthe, S., Kanakiya, S. J., Faulkner, D., Boulton, C., & Toy, V. (2017). The physical properties of Alpine Fault cataclasites that drive its elastic wave velocities. In *GSNZ Annual Conference Proceedings*: Geoscience Society of New Zealand.
- Allen, M. J., Tatham, D., Faulkner, D. R., Mariani, E., & Boulton, C. (2017). Permeability and seismic velocity and their anisotropy across the Alpine Fault, New Zealand: An insight from laboratory measurements on core from the Deep Fault Drilling Project phase 1 (DFDP-1). *Journal of Geophysical Research: Solid Earth*, 122, 6160–6179. <https://doi.org/10.1002/2017JB014355>
- Barton, C. A., Zoback, M. D., & Moos, D. (1995). Fluid flow along potentially active faults in crystalline rock. *Geology*, 23(8), 683–686. [https://doi.org/10.1130/0091-7613\(1995\)023<0683:FFAPAF>2.3.CO;2](https://doi.org/10.1130/0091-7613(1995)023<0683:FFAPAF>2.3.CO;2)
- Ben-Zion, Y. (1998). Properties of seismic fault zone waves and their utility for imaging low-velocity structures. *Journal of Geophysical Research*, 103(B6), 12,567–12,585.

- Blum, T. E., Adam, L., & van Wijk, K. (2013). Noncontacting benchtop measurements of the elastic properties of shales. *Geophysics*, 78(3), C25–C31. <https://doi.org/10.1190/geo2012-0314.1>
- Boulton, C., Moore, D. E., Lockner, D. A., Toy, V. G., Townend, J., & Sutherland, R. (2014). Frictional properties of exhumed fault gouges in DFDP-1 cores, Alpine Fault, New Zealand. *Geophysical Research Letters*, 41, 356–362. <https://doi.org/10.1002/2013GL058236>
- Bruner, W. M. (1976). Comment on 'seismic velocities in dry and saturated cracked solids' by Richard J O'Connell and Bernard Budiansk. *Journal of Geophysical Research*, 81(14), 2573–2576.
- Carpenter, B. M., Kitajima, H., Sutherland, R., Townend, J., Toy, V. G., & Saffer, D. M. (2014). Hydraulic and acoustic properties of the active Alpine Fault, New Zealand: Laboratory measurements on DFDP-1 drill core. *Earth and Planetary Science Letters*, 390, 45–51. <https://doi.org/10.1016/J.EPSL.2013.12.023>
- Christensen, N. I. (1965). Compressional wave velocities in metamorphic rocks at pressures to 10 kilobars. *Journal of Geophysical Research*, 70(24), 6147–6164.
- Christensen, N. I., & Okaya, D. A. (2007). Compressional and shear wave velocities in South Island, New Zealand rocks and their application to the interpretation of seismological models of the New Zealand crust, *Geophysical monograph series* (Vol. 175, pp. 123–155). American Geophysical Union. <https://doi.org/10.1029/175GM08>
- Cochran, U.A., Clark, K. J., Howarth, J. D., Biasi, G. P., Langridge, R. M., Villamor, P., et al. (2017). A plate boundary earthquake record from a wetland adjacent to the Alpine Fault in New Zealand refines hazard estimates. *Earth and Planetary Science Letters*, 464, 175–188. <http://doi.org/10.1016/j.epsl.2017.02.026>
- Cochran, E. S., Li, Y.-G., Shearer, P. M., Barbot, S., Fialko, Y., & Vidale, J. E. (2009). Seismic and geodetic evidence for extensive, long-lived fault damage zones. *Geology*, 37(4), 315–318.
- Dempsey, E. D., Prior, D. J., Mariani, E., Toy, V. G., & Tatham, D. J. (2011). Mica-controlled anisotropy within mid-to-upper crustal mylonites: An EBSD study of mica fabrics in the Alpine Fault Zone, New Zealand. *Geological Society, London, Special Publications*, 360(1), 33–47. <https://doi.org/10.1144/SP360.3>
- Eccles, J. D., Gulley, A. K., Malin, P. E., Boese, C. M., Townend, J., & Sutherland, R. (2015). Fault zone guided wave generation on the locked, late interseismic Alpine Fault, New Zealand. *Geophysical Research Letters*, 42, 5736–5743. <https://doi.org/10.1002/2015GL064208>
- Faulkner, D., Lewis, A., & Rutter, E. (2003). On the internal structure and mechanics of large strike-slip fault zones: Field observations of the Carboneras Fault in southeastern Spain. *Tectonophysics*, 367(3-4), 235–251.
- Gillam, B. G., Little, T. A., Smith, E., & Toy, V. G. (2014). Reprint of extensional shear band development on the outer margin of the Alpine mylonite zone, Tatare Stream, Southern Alps, New Zealand. *Journal of Structural Geology*, 64, 115–134.
- Gulley, A. K., Eccles, J. D., Kaipio, J. P., & Malin, P. E. (2017). The effect of gradational velocities and anisotropy on fault-zone trapped waves. *Geophysical Journal International*, 210(2), 964–978. <https://doi.org/10.1093/gji/ggx200>
- Hubbert, M. K., & Rubey, W. W. (1959). Role of fluid pressure in mechanics of overthrust faulting: I. Mechanics of fluid-filled porous solids and its application to overthrust faulting. *Geological Society of America Bulletin*, 70(2), 115–166.
- Jones, T., & Nur, A. (1982). Seismic velocity and anisotropy in mylonites and the reflectivity of deep crystal fault zones. *Geology*, 10(5), 260–263.
- Kelly, C. M., Faulkner, D. R., & Rietbrock, A. (2017). Seismically invisible fault zones: Laboratory insights into imaging faults in anisotropic rocks. *Geophysical Research Letters*, 44, 8205–8212. <https://doi.org/10.1002/2017GL073726>
- Kim, E., Kim, Y. H., & Mainprice, D. (2019). GassDem: A MATLAB program for modeling the anisotropic seismic properties of porous medium using differential effective medium theory and Gassmann's poroelastic relationship. *Computers and Geosciences*, 126, 131–141. <https://doi.org/10.1016/j.cageo.2019.02.008>
- Langridge, R. M., Ries, W. F., Litchfield, N. J., Villamor, P., Van Dissen, R. J., Barrell, D. J. A., et al. (2016). The New Zealand active faults database. *New Zealand Journal of Geology and Geophysics*, 59(1), 86–96. <https://doi.org/10.1080/00288306.2015.1112818>
- Li, Y.-G., Leary, P., Aki, K., & Malin, P. (1990). Seismic trapped modes in the Oroville and San Andreas fault zones. *Science*, 249(4970), 763–766.
- Li, Y.-G., Vidale, J. E., & Cochran, E. S. (2004). Low-velocity damaged structure of the San Andreas Fault at Parkfield from fault zone trapped waves. *Geophysical Research Letters*, 31, L12S06. <https://doi.org/10.1029/2003GL019044>
- Mainprice, D., Bachmann, F., Hielscher, R., Schaeben, H., & Lloyd, G. E. (2015). Calculating anisotropic piezoelectric properties from texture data using the MTEX open source package. *Geological Society, London, Special Publications*, 409(1), 223–249.
- Massiot, C., Célérrier, B., Doan, M.-L., Little, T. A., Townend, J., McNamara, D. D., et al. (2018). The Alpine Fault hangingwall viewed from within: Structural analysis of ultrasonic image logs in the DFDP-2B Borehole, New Zealand. *Geochemistry, Geophysics, Geosystems*, 19, 2492–2515. <https://doi.org/10.1029/2017GC007368>
- Mitchell, T., & Faulkner, D. (2012). Towards quantifying the matrix permeability of fault damage zones in low porosity rocks. *Earth and Planetary Science Letters*, 339, 24–31.
- Mooney, W. D., & Ginzburg, A. (1986). Seismic measurements of the internal properties of fault zones. *Pure and Applied Geophysics*, 124(1-2), 141–157.
- Norris, R. J., & Cooper, A. F. (1997). Erosional control on the structural evolution of a transpressional thrust complex on the Alpine Fault, New Zealand. *Journal of Structural Geology*, 19(10), 1323–1342.
- Norris, R. J., & Cooper, A. F. (2001). Late Quaternary slip rates and slip partitioning on the Alpine Fault, New Zealand. *Journal of Structural Geology*, 23(2-3), 507–520. [https://doi.org/10.1016/S0191-8141\(00\)00122-X](https://doi.org/10.1016/S0191-8141(00)00122-X)
- Norris, R. J., & Cooper, A. F. (2007). The Alpine Fault, New Zealand: Surface geology and field relationships. In D. Okaya, T. Stern, & F. Davey (Eds.), *A continental plate boundary: Tectonics at South Island, New Zealand* (pp. 157–175). American Geophysical Union. <https://doi.org/10.1029/175GM09>
- Norris, R. J., Koons, P. O., & Cooper, A. F. (1990). The obliquely-convergent plate boundary in the South Island of New Zealand: Implications for ancient collision zones. *Journal of Structural Geology*, 12(5-6), 715–725.
- Savage, H. M., & Brodsky, E. E. (2011). Collateral damage: Evolution with displacement of fracture distribution and secondary fault strands in fault damage zones. *Journal of Geophysical Research*, 116, B03405. <https://doi.org/10.1029/2010JB007665>
- Scholz, C. (1968). Experimental study of the fracturing process in brittle rock. *Journal of Geophysical Research*, 73(4), 1447–1454.
- Scruby, C. B., & Drain, L. E. (1990). *Laser ultrasonics: Techniques and applications*. Bristol: Adam Hilger.
- Shea, W. T., & Kronenberg, A. K. (1993). Strength and anisotropy of foliated rocks with varied mica contents. *Journal of Structural Geology*, 15(9-10), 1097–1121.
- Shipton, Z. K., Soden, A. M., Kirkpatrick, J. D., Bright, A. M., & Lunn, R. J. (2006). How thick is a fault? Fault displacement-thickness scaling revisited. In R. Abercrombie (Ed.), *Earthquakes: Radiated energy and the physics of faulting* (pp. 193–198). American Geophysical Union.

- Simpson, J. (2019). Non-contact measurements to estimate the elastic properties of rocks under in situ conditions (Masters Thesis). The University of Auckland.
- Simpson, J., Adam, L., van Wijk, K., & Charoensawan, J. (2020). Data and software for manuscript “Constraining microfractures in foliated Alpine Fault rocks with laser ultrasonics”. [https://auckland.figshare.com/collections/Data\\_and\\_software\\_for\\_manuscript\\_Constraining\\_microfractures\\_in\\_foliated\\_Alpine\\_Fault\\_rocks\\_with\\_laser\\_ultrasonics\\_4841352/1](https://auckland.figshare.com/collections/Data_and_software_for_manuscript_Constraining_microfractures_in_foliated_Alpine_Fault_rocks_with_laser_ultrasonics_4841352/1)
- Simpson, J., van Wijk, K., Adam, L., & Smith, C. (2019). Laser ultrasonic measurements to estimate the elastic properties of rock samples under in situ conditions. *Review of Scientific Instruments*, 90(11), 114503. <https://doi.org/10.1063/1.5120078>
- Sutherland, R., Townend, J., Toy, V., & DFDP-2 Science Team (2015). Deep Fault Drilling Project (DFDP), Alpine Fault boreholes DFDP-2A and DFDP-2B technical completion report, GNS Science Report 2015/50.
- Sutherland, R., Townend, J., Toy, V., Upton, P., Coussens, J., Allen, M., et al. (2017). Extreme hydrothermal conditions at an active plate-boundary fault. *Nature*, 546(7656), 137–140. <https://doi.org/10.1038/nature22355>
- Townend, J., Sutherland, R., & Toy, V. (2009). Deep Fault Drilling Project—Alpine Fault, New Zealand. *Scientific Drilling*, 8, 75–82.
- Townend, J., Sutherland, R., Toy, V. G., Eccles, J. D., Boulton, C., Cox, S. C., & McNamara, D. (2013). Late-interseismic state of a continental plate-boundary fault: Petrophysical results from DFDP-1 wireline logging and core analysis, Alpine Fault, New Zealand. *Geochemistry, Geophysics, Geosystems*, 14, 3801–3820. <https://doi.org/10.1002/ggge.20236>
- Toy, V. G., Boulton, C. J., Sutherland, R., Townend, J., Norris, R. J., Little, T. A., et al. (2015). Fault rock lithologies and architecture of the central Alpine Fault, New Zealand, revealed by DFDP-1 drilling. *Lithosphere*, 7(2), 155–173.
- Toy, V. G., Norris, R. J., Prior, D. J., Walrond, M., & Cooper, A. F. (2013). How do lineations reflect the strain history of transpressive shear zones? The example of the active Alpine Fault Zone, New Zealand. *Journal of Structural Geology*, 50, 187–198.
- Toy, V. G., Prior, D. J., & Norris, R. J. (2008). Quartz fabrics in the Alpine Fault mylonites: Influence of pre-existing preferred orientations on fabric development during progressive uplift. *Journal of Structural Geology*, 30(5), 602–621.
- Toy, V. G., Prior, D. J., Norris, R. J., Cooper, A. F., & Walrond, M. (2012). Relationships between kinematic indicators and strain during syn-deformational exhumation of an oblique slip, transpressive, plate boundary shear zone: The Alpine Fault, New Zealand. *Earth and Planetary Science Letters*, 333, 282–292.
- Toy, V. G., Sutherland, R., Townend, J., Allen, M. J., Becroft, L., Boles, A., et al. (2017). Bedrock geology of DFDP-2B, central Alpine Fault, New Zealand. *New Zealand Journal of Geology and Geophysics*, 60(4), 497–518.
- Walsh, J. (1981). Effect of pore pressure and confining pressure on fracture permeability. In *International Journal of Rock Mechanics and Mining Sciences & Geomechanics Abstracts* (Vol. 18(5), pp. 429–435).
- Walsh, J., & Brace, W. (1964). A fracture criterion for brittle anisotropic rock. *Journal of Geophysical Research*, 69(16), 3449–3456.
- Warr, L. N., & Cox, S. (2001). Clay mineral transformations and weakening mechanisms along the Alpine Fault, New Zealand. In R. E. Holdsworth, R. A. Strachan, J. F. Magloughlin, & R. J. Knipe (Eds.), *The nature and tectonic significance of fault zone weakening* (Vol. 186, pp. 85–101). Geological Society of London, Special Publications.
- Wellman, H. W. (1955). New Zealand Quaternary tectonics. *Geologische Rundschau*, 43(1), 248–257. <https://doi.org/10.1007/BF01764108>
- Wells, A., Yettton, M. D., Duncan, R. P., & Stewart, G. H. (1999). Prehistoric dates of the most recent Alpine Fault earthquakes, New Zealand. *Geology*, 27(11), 995–998. [https://doi.org/10.1130/0091-7613\(1999\)027<0995:PDOTMR>2.3.CO;2](https://doi.org/10.1130/0091-7613(1999)027<0995:PDOTMR>2.3.CO;2)
- Williams, J. N., Toy, V. G., Massiot, C., McNamara, D. D., Smith, S. A., & Mills, S. (2018). Controls on fault zone structure and brittle fracturing in the foliated hanging wall of the Alpine Fault. *Solid Earth*, 9(2), 469–489.
- Williams, J. N., Toy, V. G., Massiot, C., McNamara, D. D., & Wang, T. (2016). Damaged beyond repair? Characterising the damage zone of a fault late in its interseismic cycle, the Alpine Fault, New Zealand. *Journal of Structural Geology*, 90, 76–94. <https://doi.org/10.1016/j.jsg.2016.07.006>
- Williams, J. N., Toy, V. G., Smith, S. A., & Boulton, C. (2017). Fracturing, fluid-rock interaction and mineralisation during the seismic cycle along the Alpine Fault. *Journal of Structural Geology*, 103, 151–166.